Afterbody Flowfield Computations at Transonic and Supersonic Mach Numbers

Uriel C. Goldberg,* Joseph J. Gorski,† and Sukumar R. Chakravarthy*
Rockwell International Science Center, Thousand Oaks, California

The flowfield around various axisymmetric afterbody configurations is computed with a finite-volume Navier-Stokes code, incorporating a total variation diminishing implicit upwind-biased scheme for high accuracy and using alternatively the k-ϵ or the Baldwin-Lomax turbulence model. Computations are done for both solid plume simulators and real jet flows. Results for two geometries at several combinations of jet and freestream conditions are shown. Agreement with the experimental data is very good.

Introduction

THE pressure drag of jet engine exhaust nozzles is a prime contributor to total vehicle drag. Therefore, it is important to obtain knowledge about the afterbody flowfield in the early design stages so as to minimize the resultant drag on advanced aircraft configurations.

In the past several years, increased attention has been paid to numerical prediction methods for this problem, in an effort to avoid the complexity, limitations, and high cost of wind tunnel testing. However, reliable computational methods treating transonic freestream conditions and incorporating real plume effects have only recently begun to appear.[1-7]

In this flow regime, strong viscous-inviscid and viscous-viscous interactions occur and the pressure drag on the afterbody surface must, therefore, be computed with the mutual effects of exhaust jet and outer stream fully taken into consideration. Figure 1 is a schematic view of the transonic afterbody flowfield, indicating typical flow phenomena such as normal shock formation and its interaction with the boundary layer (including possible separation), plume blockage, and plume entrainment.

In order to compute this complex flowfield, the full Navier-Stokes equations must be used, thus simultaneously solving the inviscid and viscous regions with no matching requirements. In the present work, the time-dependent, compressible Reynolds-averaged Navier-Stokes equations were solved for the entire axisymmetric nozzle/afterbody flowfield, using alternatively the k-ϵ or the Baldwin-Lomax turbulence model, the former with a new near-wall treatment.[8] A finite-volume code, incorporating a highly accurate total variation diminishing (TVD) implicit upwind-biased scheme, has been used for the flow computations.[9,10]

The present work demonstrates the capabilities of the code in the prediction of nozzle/afterbody external pressure distributions, as compared with experimental data[11-13] for two geometries with several combinations of jet and freestream conditions. Calculations are presented for both plume simulators and real jet flows, where the plume development is part of the solution.

Presented as Papers 85-1639 and 85-4081 at the AIAA 18th Fluid Dynamics and Plasmadynamics and Lasers Conference, Cincinnati, OH, July 16-18, 1985 and the AIAA 3rd Applied Aerodynamics Conference, Colorado Springs, CO, Oct. 14-16, 1985; received Oct. 26, 1985; revision received July 21, 1986.

*Member Technical Staff. Member AIAA.
†Senior Technical Specialist. Member AIAA.

Problem Formulation

To formulate the problem, the computational domain is chosen first, followed by a choice of gridding with appropriate clustering to capture regions where high gradients occur. A body-fitted coordinate system is employed through numerical mapping. Next, the equations of motion for compressible, turbulent flow are solved in the transformed plane, subject to specified boundary conditions, and using either the k-ϵ or the Baldwin-Lomax turbulence model. Details of this procedure are given below.

Computational Domain

Figures 2a and 2b show the two geometries used in the present computations. More details may be found in Refs. 11-13. The corresponding computational domains and gridding approaches are shown in Figs. 3a and 3b. In the case of the solid plume simulator (Fig. 3a), the boattail arc is between $x=0.0$ and $x=0.80$. A 65×40 grid was used for the computations. All dimensions in this case are referenced to the basic afterbody diameter D indicated in Fig. 2a. In the case of real jet flow (Fig. 3b), the boattail is between $x=0.0$ and $x=2.846$. A 60×25 "C" grid was used here. All dimensions in this case are referenced to the nozzle throat radius R_t indicated in Fig. 2b. An exponential stretching was used for both grids, with 10-15 points within the shear layers.

Coordinate System

An axisymmetric coordinate system is used (see Fig. 3), with u and v being the velocity components along the axial direction x and the radial direction y, respectively. These coordinates are transformed into a (ξ,η) system that maps the computational region into a rectangle, with constant η lines approximately parallel to the body surface and constant ξ lines approximately normal to it.

Equations of Motion

The compressible, Reynolds-averaged Navier-Stokes equations for axisymmetric flow are written in the following conservation form, where the dependent variables u, v, and e are mass averaged, with e being the specific total internal energy, T the temperature, ρ and p the mean density and pressure, respectively, and t the time:

$$\frac{\partial W}{\partial t}+\frac{\partial F}{\partial x}+\frac{\partial G}{\partial y}+\frac{G}{y}=\frac{H}{y} \tag{1a}$$

and

$$W=\begin{bmatrix}\rho\\ \rho u\\ \rho v\\ \rho e\end{bmatrix},\quad F=\begin{bmatrix}\rho u\\ \rho u^2-\sigma_{xx}\\ \rho uv-\tau_{xr}\\ \rho ue+\dot{q}_x-\sigma_{xx}u-\tau_{xr}v\end{bmatrix}$$

$$G=\begin{bmatrix}\rho v\\ \rho uv-\tau_{xr}\\ \rho v^2-\sigma_{rr}\\ \rho ve+\dot{q}_r-\tau_{xr}u-\sigma_{rr}v\end{bmatrix},\quad H=\begin{bmatrix}0\\ 0\\ -\sigma_+\\ 0\end{bmatrix} \tag{1b}$$

where

$$\sigma_{xx}=-p-\frac{2}{3}(\mu+1\mu_t)\nabla\cdot U+2(\mu+\mu_t)\frac{\partial u}{\partial x}$$

$$\sigma_{rr}=-p-\frac{2}{3}(\mu+1\mu_t)\nabla\cdot U+2(\mu+\mu_t)\frac{\partial v}{\partial y}$$

$$\sigma_+=-p-\frac{2}{3}(\mu+1\mu_t)\nabla\cdot U+2(\mu+\mu_t)\frac{v}{y}$$

$$\tau_{rx}=\tau_{xr}=(\mu+\mu_t)\left(\frac{\partial u}{\partial y}+\frac{\partial v}{\partial x}\right)$$

$$e=C_vT+\tfrac{1}{2}(u^2+v^2)$$

$$\dot{q}_x=-C_p\left(\frac{\mu}{Pr}+\frac{\mu_t}{Pr_t}\right)\frac{\partial T}{\partial x}$$

$$\dot{q}_r=-C_p\left(\frac{\mu}{Pr}+\frac{\mu_t}{Pr_t}\right)\frac{\partial T}{\partial y}$$

$$\nabla\cdot U=\frac{\partial u}{\partial x}+\frac{\partial v}{\partial y}+\frac{v}{y} \tag{1c}$$

The air was assumed to be a perfect gas for both internal and external flows, satisfying the equation of state

$$p=\rho RT \tag{2}$$

For the dependence of molecular viscosity on temperature, either a power law or Sutherland's law was used,

$$\mu/\mu_0=(T/T_0)^n$$

or

$$=(T/T_0)^{3/2}(T_0+S)/(T+S) \tag{3}$$

with $\mu_0=0.1716mP, 0.67\le n\le 1$, $T_0=491.6°\text{R}$, and $S=199°\text{R}$. μ in Eq. (1c) denotes the eddy viscosity.

The laminar and turbulent Prandtl numbers, Pr and Pr_t, were assumed constant with values of 0.72 and 0.9, respectively. The ratio of specific heats γ was also assumed constant and equal to 1.4. C_v and C_p are specific heat capacities at constant volume and constant pressure, respectively.

In the ϵ-η computational plane, Eq. (1a) is transformed into the finite-volume conservation law form represented by[10]

$$\frac{\partial W}{\partial\tau}+\frac{1}{\text{area}}\left[(y_\eta F-x_\eta G)_\xi+(-y_\xi F+x_\xi G)_\eta+\frac{G}{y}-\frac{H}{y}\right]=0 \tag{4}$$

where ξ and η are the new independent variables and x_ξ, x_η, y_ξ, and y_η the four transformation coefficients obtained numerically from the mapping procedure. The "area" in Eq. (4) denotes that of the finite-volume cell under consideration at the time of discretization of the equations, τ denotes the transformed time.

k-ϵ Turbulence Modeling

The experiments used here for comparisons with the computations were run at Reynolds numbers per meter on the order of 10^7. Therefore, the flow was fully turbulent. In the present work, either the k-ϵ or the Baldwin-Lomax model of turbulence was used. The latter model is well known and will not be described here. The k-ϵ model for axisymmetric flow is written in a normalized form as

$$\frac{\partial A}{\partial t}+\frac{\partial B}{\partial x}+\frac{\partial C}{\partial y}=\frac{1}{Re}\left(\frac{\partial M}{\partial x}+\frac{\partial N}{\partial y}+S+D_A\right) \tag{5a}$$

where Re is the reference Reynolds number,

$$A=\begin{bmatrix}\rho k\\ \rho\epsilon\end{bmatrix},\quad B=\begin{bmatrix}\rho uk\\ \rho u\epsilon\end{bmatrix},\quad C=\begin{bmatrix}\rho vk\\ \rho v\epsilon\end{bmatrix}$$

$$M=\begin{bmatrix}\mu_k\dfrac{\partial k}{\partial x}\\ \mu_\epsilon\dfrac{\partial\epsilon}{\partial x}\end{bmatrix},\quad N=\begin{bmatrix}\mu_k\dfrac{\partial k}{\partial y}\\ \mu_\epsilon\dfrac{\partial\epsilon}{\partial y}\end{bmatrix}$$

$$S=\begin{bmatrix}P-\rho\epsilon Re\\ C_1\dfrac{y\epsilon}{k}P-C_2\rho\dfrac{\epsilon^2}{k}Re\end{bmatrix},\quad D_A=\begin{bmatrix}\dfrac{\mu_k}{y}\dfrac{\partial k}{\partial y}-\dfrac{\rho vk}{y}Re\\ \dfrac{\mu_\epsilon}{y}\dfrac{\partial\epsilon}{\partial y}-\dfrac{\rho v\epsilon}{y}Re\end{bmatrix}$$

and

$$\mu_k=(\mu+\mu_t/\sigma_k)$$

$$\mu_\epsilon=(\mu+\mu_t/\sigma_\epsilon)$$

P represents the production of turbulence kinetic energy and the following simplified form of it is used here:

$$P=\mu_t(u_y+v_x)^2 \tag{5b}$$

The eddy viscosity is given by

$$\mu_t=C_\mu\rho(k^2/\epsilon) \tag{5c}$$

where k is the turbulence kinetic energy and ϵ its dissipation. The constants used in this model are $\sigma_k=1.0$, $\sigma_\epsilon=1.3$,

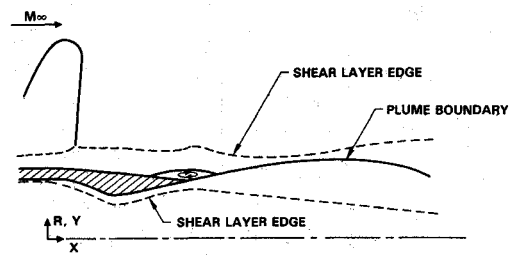

Fig. 1 Schematic view of transonic nozzle/afterbody flowfield.

$C_1 = 1.44$, $C_2 = 1.92$, and $C_\mu = 0.09$. The k-ϵ equations follow the same general form as the Navier-Stokes equations save for the source terms. Consequently, the same numerical treatment applied to solve the Navier-Stokes equations has also been applied to solve the k-ϵ equations.[9]

Boundary Conditions

Since the unsteady Navier-Stokes and k-ϵ equations are solved, both initial and boundary conditions are required.

Upstream Boundaries

Inviscid inflow and stagnation conditions are specified at the external and internal (jet) upstream boundaries, respectively, and are held fixed during the solution procedure. This approach is adequate for pressure predictions, but may not enable the correct boundary-layer development necessary for predictions of skin friction and heat transfer. This stems from the fact that the real inflow has a finite boundary-layer thickness that will dictate normal-to-wall gradients different from those evolving from the currently used inviscid inflow.

Outer Boundary

The outer (far-field) boundary must allow mass flow to cross. This is achieved by imposing left- or right-running characteristic wave inflow or outflow boundary conditions using Riemann invariants, which depend on the number of positive and negative eigenvalues. For details, see Refs. 14 and 15.

Downstream Boundary (Solid Plume Case)

The downstream boundary is placed far enough away from the boattail for streamwise gradients to become insignificant; thus, nonreflective radiation boundary conditions are imposed there.

Centerline Boundary

Since the centerline is a line of symmetry, neither mass nor energy crosses it. This is imposed by requiring vanishing of the normal velocity component v and symmetry conditions for u, ρ and p along the centerline.

Solid Walls

The internal and external walls (including plume simulator) are treated as no-slip, impermeable and adiabatic boundaries. In addition, the normal pressure gradient is set to zero at the walls.

Initial Conditions

One-seventh power law velocity profiles are set as initial conditions for both internal and external flowfields. A parabolic pressure distribution, varying from stagnation, through choking, to ambient values, is imposed along the nozzle for the real jet flow case. Freestream pressure is imposed on the external flowfield. All other flow parameters are set through isentropic relations.

For k and ϵ, typical values are set at the first mesh points outside the viscous sublayers (see next section) and are then linearly varied with distance from walls.

k-ϵ Boundary Conditions

Since Eq. (5a) is not valid in the vicinity of solid surfaces, a near-wall treatment is necessary to provide k and ϵ adjacent to walls, as well as to provide boundary conditions for Eq. (5a), which is solved away from walls. The method of Ref. 8 is used here and the reader is referred to that paper for a detailed discussion.

Numerical Procedure

A finite-volume time-marching code, incorporating an implicit upwind scheme, Gauss-Seidel line relaxation, and total

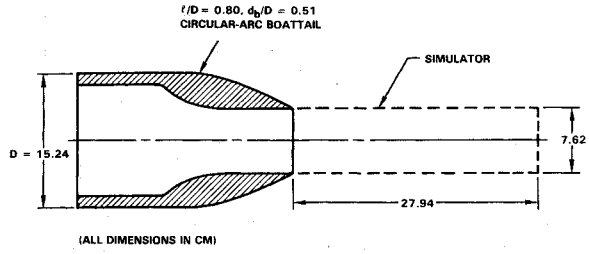

Fig. 2a Afterbody with solid plume simulator (configuration 1 of Ref. 12; all dimensions are in centimeters).

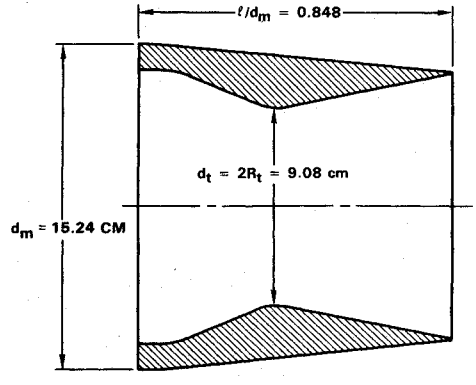

Fig. 2b Nozzle/afterbody (configuration P-1.69-S of Ref. 13; all dimensions are in centimeters).

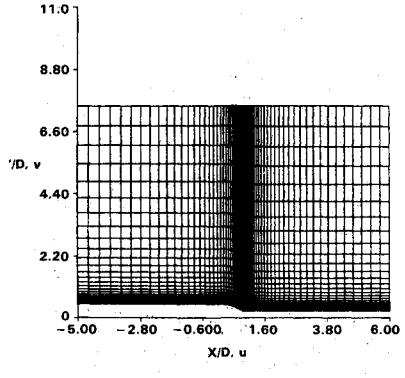

Fig. 3a Computational grid for configuration 1 of Ref. 12 with solid plume simulator.

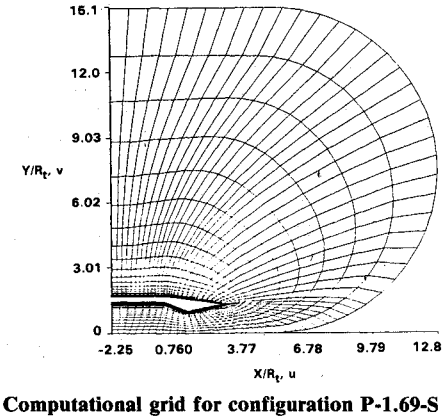

Fig. 3b Computational grid for configuration P-1.69-S of Ref. 13.

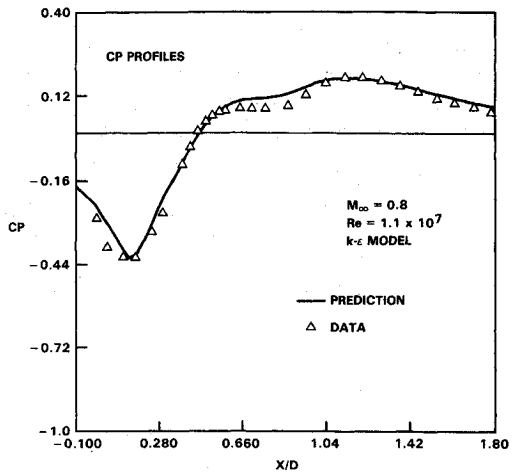

Fig. 4 Comparison between prediction and data of pressure coefficient for configuration 1 of Ref. 12 at $M_\infty = 0.8$, $Re = 1.1 \times 10^7$, using k-ϵ turbulence model.

variation diminishing (TVD) discretization with third-order accuracy, has been used to solve the Navier-Stokes and k-ϵ equations. The two sets of equations were solved in a decoupled manner with each set using the most updated information from the other. The dissipation terms were treated more or less conventionally, using central difference approximations for all second derivative terms, except for the cross-derivative terms, which were handled in a special way to augment diagonal dominance. Further details pertaining to the numerical procedure are given in Refs. 9, 10, and 14–16. The VAX 11/780 computer was used to generate the results reported in this work.

Results

Results are now presented for both plume simulator and real jet flow cases, spanning the transonic-to-supersonic flow regime.

General Observations

A rather crude grid was employed for all the computations. This prevented accurate skin-friction prediction, since there was not enough near-wall resolution to accurately compute normal-to-wall velocity gradients. Thus, the outer wall skin-friction plots shown here are included only to indicate trends, such as the absence or presence of separation and its approximate location and extent. In spite of the coarse grids used, the contour plots demonstrate sharpness of detail afforded by the high accuracy TVD scheme; shocks, nozzle flow details, plume development, and its influence on the flow, are all captured very clearly. Outer wall pressure distributions generally compare very well with the experimental data in all cases. Two problematic zones are large separated regions and the trailing edge of the internal/external flow geometry. The present turbulence models are not rich enough to provide accurate details of turbulence quantities in the presence of separation, the main reasons being the inadequacy of the law of the wall and the employment of wrong length and stress scales. Improved near-wall and backflow modeling[17,18] and introduction of an algebraic Reynolds stress model should enhance the turbulence prediction capability for separated flows. Switching to a multizone gridding approach will increase gridding flexibility and will enable better resolution of the trailing-edge region, which is difficult to achieve with a "C" type of grid.

Solid Plume Simulator

The computational procedure described in the previous sections has been used to calculate the external flowfield of the boattail/plume simulator shown in Figs. 2a and 3a. External pressure predictions have been compared with the experimental data of Refs. 11 and 12 for two transonic freestream Mach

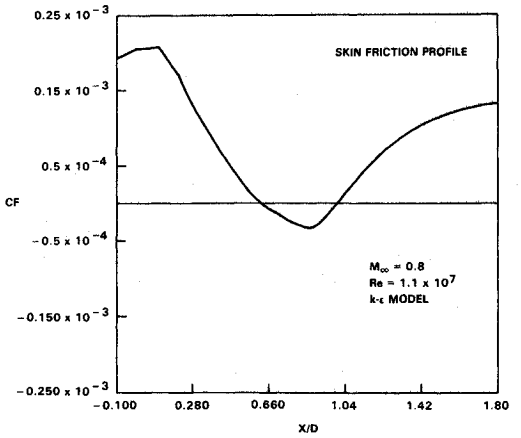

Fig. 5 Prediction of skin friction for the configuration and flow conditions of Fig. 4.

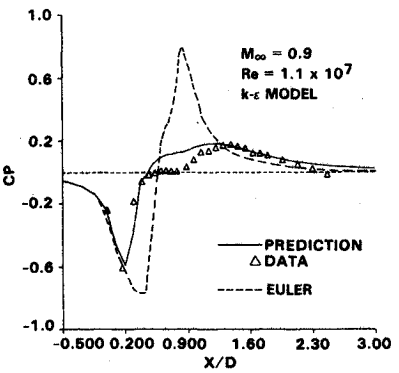

Fig. 6 Comparison between predictions and data of pressure coefficient for configuration 1 of Ref. 12.

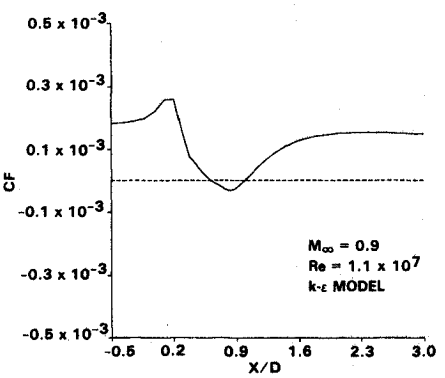

Fig. 7 Prediction of skin friction for the configuration and flow conditions of Fig. 6.

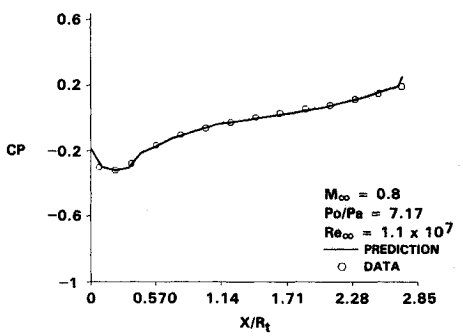

Fig. 8 Outer wall pressure distribution at $M_\infty = 0.8$.

numbers. The k-ϵ turbulence model was used for all solid plume computations. Figure 4 compares the predicted wall pressure coefficient distribution with experimental data for $M_\infty = 0.8$ and Fig. 5 shows the corresponding skin-friction prediction. The separated region indicated in Fig. 5 agrees rather well with the pressure plateau seen in Fig. 4. Figures 6 and 7 correspond to the same configuration as that of Figs. 4 and 5 for $M_\infty = 0.9$. Figure 6 includes an Euler prediction, which demonstrates very clearly the importance of viscous phenomena in flows of this type. The location and extent of separation in Fig. 7 again agrees quite well with the pressure plateau of Fig. 6.

Real Jet Flow

The experimental data of Ref. 13 have been used to check the performance of the Navier-Stokes code. The geometry chosen for data comparisons is shown in Figs. 2b and 3b. Two transonic and two supersonic flow conditions were picked: $M_\infty = 0.8$ with nozzle total to ambient pressure ratio of 7.17, $M_\infty = 0.9$ with a pressure ratio of 7.82, $M_\infty = 1.2$ with a pressure ratio of 7.81, and $M_\infty = 2.16$ with a pressure ratio of 7.75. The transonic cases were computed using the k-ϵ model, while the supersonic ones utilized the Baldwin-Lomax model of turbulence. This choice resulted from the observation that the latter did an inferior performance for transonic flows, as compared to the k-ϵ model. Since the supersonic cases are computationally less demanding, it was felt that the Baldwin-Lomax model might be better suited for those flows.

Calculated pressure distribution is compared with data in Fig. 8 for the $M_\infty = 0.8$ case. Mach and pressure contours are

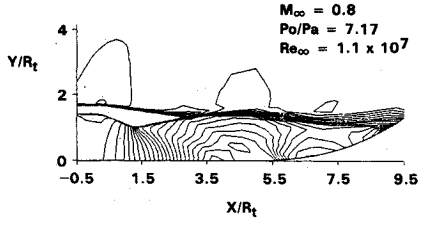

Fig. 9 Mach contours for the $M_\infty = 0.8$ case.

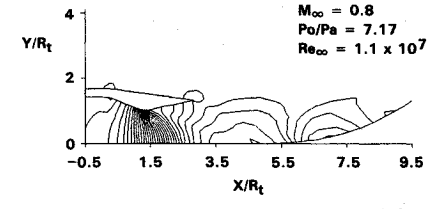

Fig. 10 Pressure contours for the $M_\infty = 0.8$ case.

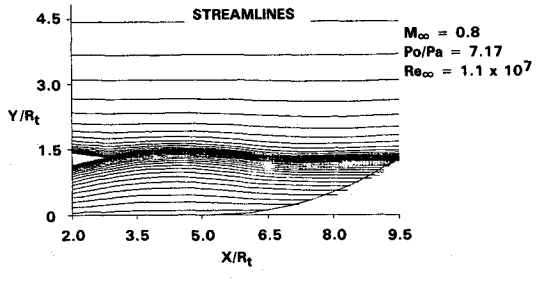

Fig. 11 Near-wake streamline plot for the $M_\infty = 0.8$ case.

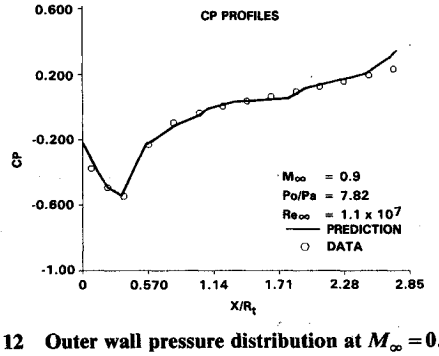

Fig. 12 Outer wall pressure distribution at $M_\infty = 0.9$.

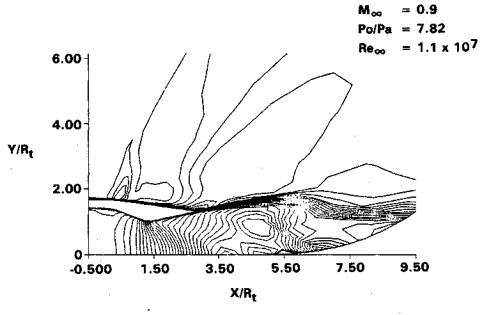

Fig. 13 Mach contours for the $M_\infty = 0.9$ case.

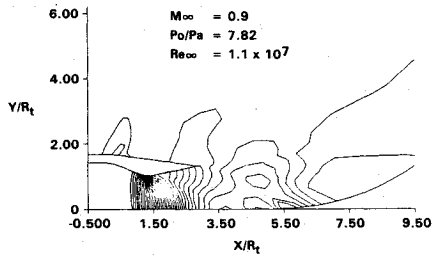

Fig. 14 Pressure contours for the $M_\infty = 0.9$ case.

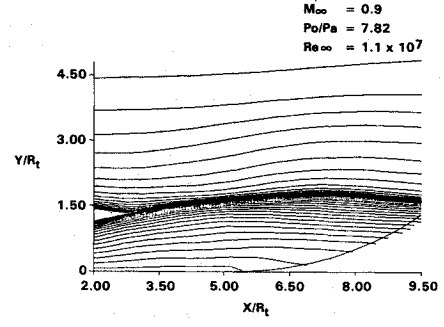

Fig. 15 Near-wake streamline plot for the $M_\infty = 0.9$ case.

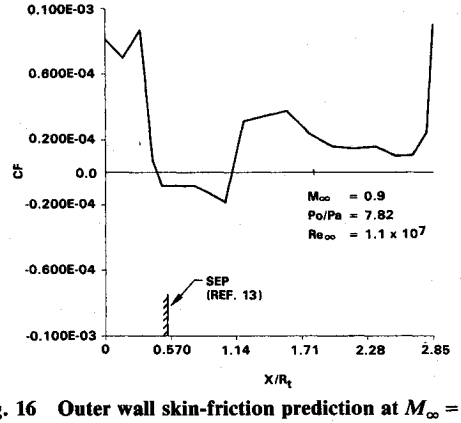

Fig. 16 Outer wall skin-friction prediction at $M_\infty = 0.9$.

shown in Figs. 9 and 10, respectively. The streamline behavior in the boattail trailing-edge and near-wake region, shown in Fig. 11, gives a clear picture of the plume development.

The $M_\infty = 0.9$ case is more difficult to predict because the normal shock impinging on the boattail separates the flow. Computed pressure distribution comparison with data is shown in Fig. 12. Mach and pressure contours are shown in Figs. 13 and 14, while the near-wake plume behavior is shown in the streamline plot of Fig. 15. Skin friction is depicted in Fig. 16, showing the approximate location and extent of the separated region. The location of separation as given in Ref. 13 is also indicated in the figure. Agreement is good.

The predicted external pressure distribution is compared with data in Fig. 17 for the $M_\infty = 1.2$ case. Figures 18 and 19 show the corresponding Mach and pressure contours, respectively, and Fig. 20 shows external skin friction, indicating separation over the downstream portion of the boattail. Figure 21 compares calculated pressure distribution with data for $M_\infty = 2.16$, while Figs. 22 and 23 show the corresponding Mach and pressure contour plots. In both supersonic cases, separation is induced by an oblique shock, seen in the contour plots (Figs. 18, 19, 22, and 23).

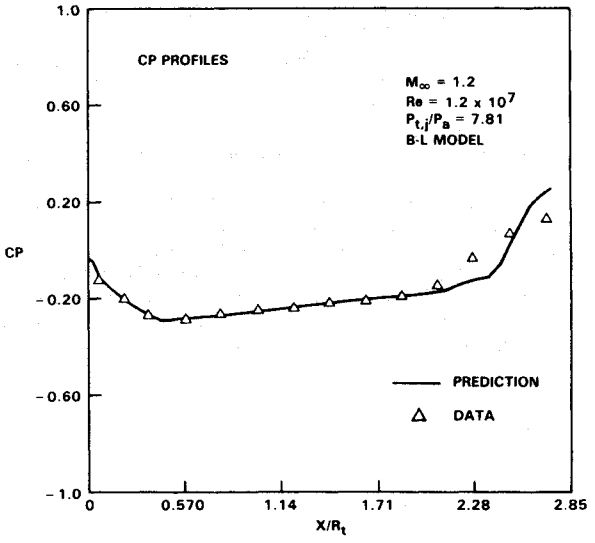

Fig. 17 Comparison between prediction and data of C_p for $M_\infty = 1.2$ (Baldwin-Lomax turbulence model used).

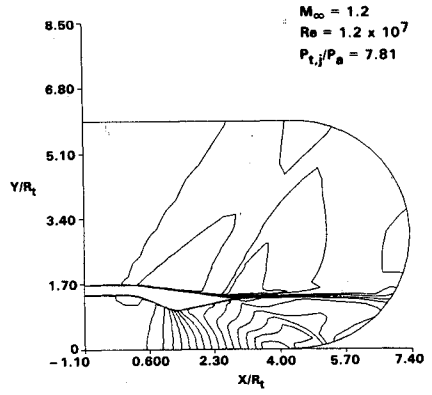

Fig. 18 Mach contours for configuration P-1.69-S of Ref. 13 at $M_\infty = 1.2$, $Re = 1.2 \times 10^7$, and $P_{t,j}/P_a = 7.81$.

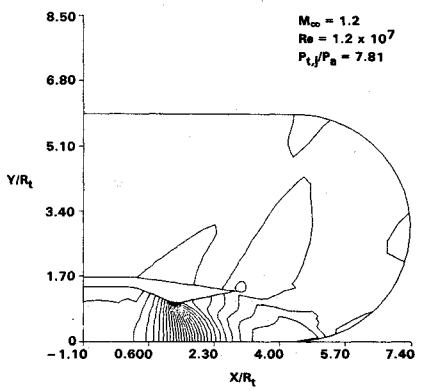

Fig. 19 Pressure contours for the $M_\infty = 1.2$ case.

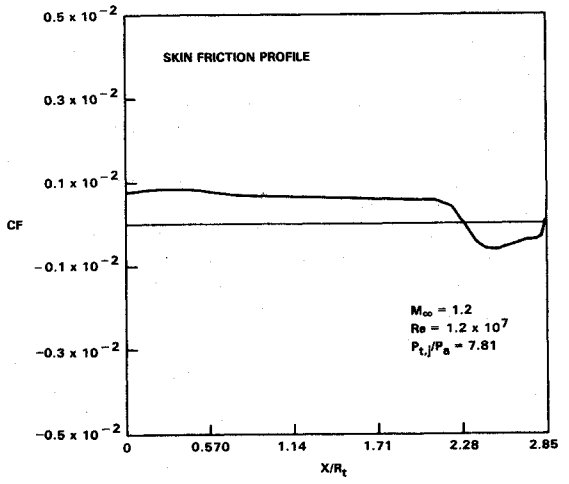

Fig. 20 Prediction of skin friction for the $M_\infty = 1.2$ case.

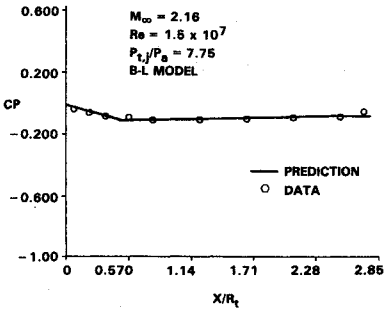

Fig. 21 Comparison between prediction and data of C_p for $M_\infty = 2.16$ (Baldwin-Lomax turbulence model used).

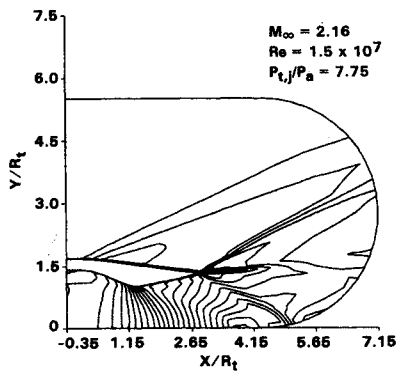

Fig. 22 Mach contours for configuration P-1.69-S of Ref. 13 at $M_\infty = 2.16$, $Re = 1.5 \times 10^7$, and $P_{t,j}/P_a = 7.75$.

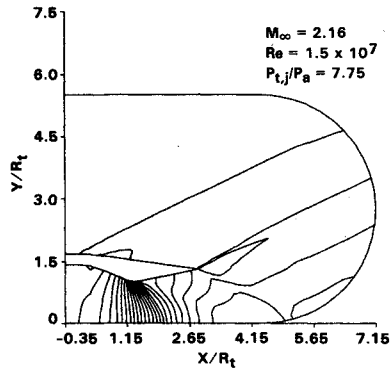

Fig. 23 Pressure contours for the $M_\infty = 2.16$ case.

Conclusions

A finite-volume computer code for the Navier-Stokes equations has been applied to the problem of transonic and supersonic flow past axisymmetric afterbodies. Turbulence was simulated using the k-ϵ equations with a new near-wall treatment for the transonic cases, while the Baldwin-Lomax model was used for the supersonic ones. For the convection parts of the Navier-Stokes and k-ϵ equations, a high-accuracy TVD scheme was used to discretize the equations. A line relaxation approach was used for the solution of the discrete system of equations. There are no numerical "tuning knobs" in the code and, thus, no such parameters were changed for any of the computations.

The agreement between data and predictions demonstrates the predictive capability of this code, rendering it a strong candidate for engineering analysis and design purposes.

References

[1]Cline, M. C. and Wilmoth, R. G., "Computation of High Reynolds Number Internal/External Flows," AIAA Paper 81-1194, June 1981.

[2]Jacocks, J. L., Peters, W. L., and Guyton, F. C., "Comparison of Computational and Experimental Jet Effects," *Journal of Aircraft*, Vol. 19, Nov. 1982, pp. 963–968.

[3]Mace, J. L. and Cosner, R. R., "Analysis of Viscous Transonic Flow over Aircraft Forebodies and Afterbodies," AIAA Paper 83-1366, June 1983.

[4]Kern, P. R. A. and Hopcroft, R. G., "Progress Toward the Analysis of Complex Propulsion Installation Flow Phenomenon," AIAA Paper 83-1367, June 1983.

[5]Deiwert, G. S., "Supersonic Axisymmetric Flow over Boattails Containing a Centered Propulsive Jet," *AIAA Journal*, Vol. 22, Oct. 1984, pp. 1358–1365.

[6]Goldberg, U. C., Gorski, J. J., and Chakravarthy, S. R., "Transonic Turbulent Flow Computations for Axisymmetric Afterbodies," AIAA Paper 85-1639, 1985.

[7]Goldberg, U. C., Gorski, J. J., and Chakravarthy, S. R., "Flow Field Computations around Nozzle/Afterbody Configurations at Transonic Mach Numbers," AIAA Paper 85-4081, 1985.

[8]Gorski, J. J., "A New Near Wall Formulation for the k-ϵ Equations of Turbulence," AIAA Paper 86-0556, 1986.

[9]Gorski, J. J., Chakravarthy, S. R., and Goldberg, U. C., "High Accuracy TVD Schemes for the k-ϵ Equations of Turbulence," AIAA Paper 85-1665, 1985.

[10]Chakravarthy, S. R., Szema, K.-Y., Goldberg, U. C., Gorski, J. J., and Osher, S., "Application of a New Class of High Accuracy TVD Schemes to the Navier-Stokes Equations," AIAA Paper 85-0165, Jan. 1985.

[11]Reubush, D. E., "Experimental Study of the Effectiveness of Cylindrical Plume Simulators for Predicting Jet-On Boattail Drag at Mach Numbers up to 1.30," NASA TN D-7795, Nov. 1974.

[12]Abeyounis, W. K. and Putnam, L. E., "Investigation of the Flow-Field Surrounding Circular-Arc Boattail Nozzles at Subsonic Speeds," NASA TP 1633, May 1980.

[13]Berrier, B. L. and Re, R. J., "Investigation of Convergent-Divergent Nozzles Applicable to Reduced-Power Supersonic Cruise Aircraft," NASA TP 1766, 1980.

[14]Chakravarthy, S. R. and Osher, S., "Numerical Experiments with the Osher Upwind Scheme for the Euler Equations," *AIAA Journal*, Vol. 21, Sept. 1983, pp. 1241-1248.

[15]Chakravarthy, S. R., "Euler Equations—Implicit Schemes and Boundary Conditions," *AIAA Journal*, Vol. 21, May 1983, pp. 699–706.

[16] Chakravarthy, S. R., "Relaxation Methods for Unfactored Implicit Upwind Schemes," AIAA Paper 84-0165, 1984.

[17]Goldberg, U. C., "Separated Flow Treatment with a New Turbulence Model," *AIAA Journal*, Vol. 24, Oct. 1986, pp. 1711-1713.

[18]Goldberg, U. C., "Separated Flow Calculations with a New Turbulence Model," Paper presented at 1st World Congress on Computational Mechanics, Austin, TX, Sept. 1986.